NACA

CASE FILE
COPY

RESEARCH MEMORANDUM

INVESTIGATION OF TWO-STAGE COUNTERROTATING COMPRESSOR

III - DESIGN OF SECOND-STAGE ROTOR AND PRELIMINARY

OVER-ALL PERFORMANCE

By Ward W. Wilcox and Linwood C. Wright

Lewis Flight Propulsion Laboratory
Cleveland, Ohio

CLASSIFICATION CHANGED TO UNCLASSIFIED
AUTHORITY: NASA PUBLICATION ANNOUNCEMENT NO. 4 WHL
EFFECTIVE DATE FEBRUARY 10, 1959

NATIONAL ADVISORY COMMITTEE
FOR AERONAUTICS
WASHINGTON
October 22, 1956

CONFIDENTIAL

NATIONAL ADVISORY COMMITTEE FOR AERONAUTICS

RESEARCH MEMORANDUM

INVESTIGATION OF TWO-STAGE COUNTERROTATING COMPRESSOR

III - DESIGN OF SECOND-STAGE ROTOR AND PRELIMINARY OVER-ALL PERFORMANCE

By Ward W. Wilcox and Linwood C. Wright

SUMMARY

In an investigation of the performance of a two-stage counterrotating compressor, an over-all average pressure ratio of 4.3 was obtained with both rotors at design speed at a specific weight flow of 27.2 pounds per second per square foot of frontal area with an adiabatic efficiency of 0.75.

Preliminary tests indicate that a weight-flow mismatching exists between the two rotors, which causes the first-stage rotor to operate at less than peak efficiency at design speed. At lower speeds, the first stage operated in the stall region fixed by single-stage tests. With the second rotor installed, no periodic rotating stall was observed, although random fluctuations of similar magnitude were noted.

INTRODUCTION

The design and over-all performance of the first stage of a two-stage counterrotating compressor are reported in reference 1. As pointed out in reference 2, this rotor was a highly loaded transonic blade row. The second-stage rotor has characteristics unique to counterrotation that must be accounted for in its design. Although the second-stage rotor has inlet relative Mach numbers in the high supersonic region, its actual tip speed is fairly low and the equivalent tip speed even lower because of energy addition in the first rotor. High inlet relative Mach numbers and high air-flow angles are inherent in the design of this counterrotating stage. In addition, supersonic rotors characteristically have a narrow operating range, so that close matching with the first stage is required for optimum performance.

· This report outlines the design procedure used for the second-stage supersonic compressor rotor and includes the results of preliminary tests on the stages in combination.

CONFIDENTIAL

SYMBOLS

A_F frontal area of first rotor, sq ft

a   speed of sound

b   annulus height

c_p specific heat at constant pressure

$\mathscr{F}$ force term

g   acceleration due to gravity, 32.17 ft/sec^2

H   total enthalpy

M   Mach number

ΔM $M_s - M_p$

N   rotational speed, rpm

n   number of blades

P   total pressure

p   static pressure

R   gas constant, 1716 ft-lb/(slug)(^{O}R)

r   radius, in.

S   entropy

T   total temperature, ^{O}R

t   stream (static) temperature, ^{O}R

V   velocity, ft/sec

w   weight flow through annulus bordered by r_t and r, lb/sec

w_{tot} total weight flow, lb/sec

z   axial distance, in.

β   air angle, angle between air velocity and axial direction, deg

γ ratio of specific heats

δ ratio of inlet pressure to NACA standard sea-level pressure

ζ weight-flow correction parameter

η_{ad} adiabatic efficiency

Θ angular coordinate

θ ratio of inlet temperature to NACA standard sea-level temperature of 518.7° R

$\varkappa$ blade angle, angle between tangent to blade mean camber line and axial direction, deg

ρ stream (static) density

σ_z solidity, ratio of axial length to spacing

τ thickness normal to mean line, in.

τ_θ thickness normal to axis, in.

ω angular velocity, radians/sec

Subscripts:

a   stagnation conditions

corr   corrected

h   hub

int   integrated

n,n+1   radial stations, n at tip

o   original

p   pressure surface

r   radial

s   suction surface

t   tip

tot   total

x   station along axis

z   axial

θ tangential

0   compressor inlet

1   first-rotor inlet

2   first-rotor outlet

2a   second-rotor inlet

3   second-rotor outlet

Superscripts:

'   relative to rotor

—   average

DESIGN OF SECOND-STAGE ROTOR

Over-All Conditions

Initially, a pressure ratio of about 5 at a specific equivalent
weight flow of 30 pounds per second per square foot of frontal area was
chosen as the design goal for the counterrotating compressor. From tur-
bine considerations a work split of 1 to 2 for first and second stages,
respectively, was selected. Because angular speed of the two rotors was
maintained equal, the actual design tip speed for the smaller-diameter
second rotor was 1198 feet per second compared with 1260 feet per second
for the first-stage rotor. Also, because of the temperature rise from
the first rotor the equivalent (based on second-stage inlet) tip speed of
the second rotor was 1075 feet per second. Design pressure ratio for the
second stage was 2.63, and average efficiency was assumed to be 0.85.

Rotor-Inlet Conditions

Design inlet conditions for the second-stage rotor were determined by
the interrotor design calculation outlined in appendix B of reference 1.
This calculation established the design conditions at the outlet of the
first stage and also accounted for the changes in the annulus between
rotors. Flow conditions were found at the three axial stations A, B, and
C shown in the sketch of figure 1. To avoid choking in the converging

annulus, the distance between rotors was kept small, in this case 3/4 inch at the hub. Exact design flow conditions at the rotor leading edge were found by interpolation between stations B and C of figure 1. In the radial direction, all parameters were plotted against percent weight flow from the outer casing, 100-percent weight flow setting the inlet hub radius. The important design parameters for the vector diagrams of both rotors are given in table I for the hub-, mean-, and tip-radius elements (100, 50, and 0% flow, respectively).

Outline of Design Method

To fix the exact design of the second-stage rotor, the outlet thermo-dynamic conditions were first established at the desired level. Next, the over-all total-pressure ratio was divided by the first-stage pressure ratio to determine the required contribution of the second stage. These parameters were assumed to be direct functions of weight flow from the outer casing and implicit functions of the radius. To determine the out-let hub radius and the radii at various streamlines, as designated by per-cent mass flow, a radially stepwise solution of the equation of motion and the energy equation was used. These equations, together with the continuity equation, also yielded the outlet velocity components. An arbitrary hub shape satisfying the known slope and radius at inlet and outlet was then assigned. The mean-radius blade camber line was deter-mined from blade-loading considerations, as was the thickness. The thick-ness perpendicular to the axis of rotation τ_θ was held constant with radius, and separate camber lines for hub and tip were determined to sat-isfy inlet and outlet diagrams. In addition, a correction was applied to blade thickness at all radii to account for the overestimation of ρV occurring when average Mach numbers are near unity. Details of the design procedure follow.

Details of Second-Stage Rotor Design

Over-all thermodynamic conditions. - The radial variation of over-all pressure ratio shown in figure 2(a) was assumed. From this assumed pressure ratio and the design first-stage pressure ratio, the second-stage pressure ratio (fig. 2(b)) was determined. In addition, the second-stage radial variation of efficiency shown in figure 2(b) was also assumed, with an average value of about 0.85. The individual element efficiencies were maintained at or below the efficiency corresponding to normal-shock losses at the inlet relative Mach number.

The temperature-rise ratio across the second stage is given as

$$\frac{T_3}{T_2} = \frac{1}{\eta_{ad}}\left[\left(\frac{P_3}{P_2}\right)^{\frac{\gamma-1}{\gamma}} - 1 + \eta_{ad}\right] \tag{1}$$

where $T_2 = 645^\circ$ R. Then the entropy increase is

$$\Delta S = R \ln \left[\frac{\left(\frac{T_3}{T_2}\right)^{\frac{\gamma}{\gamma-1}}}{\frac{P_3}{P_2}} \right] \qquad (2)$$

and the corresponding absolute tangential velocity at the tip is

$$V_{\theta,3} = \left[\frac{c_p}{\omega} (T_3 - T_2) + (rV_\theta)_2 \right] \frac{1}{r_t} \qquad (3)$$

Rotor-exit diagrams and hub radius. - With the thermodynamic changes across the second rotor fully determined as functions of percent weight flow from the tip, it was necessary to determine the required blade shape, hub exit radius, and hub contour. The first step requires the determination of rotor-exit flow velocity diagrams and the radius at which each would exist. This can be done through stepwise solution inward along the rotor-exit blade span of the radial component of the equation of motion (ref. 3). Given in complete form for nonviscous flow, this equation is

$$\frac{\partial H}{\partial r} = \mathscr{F}_r + t \frac{\partial S}{\partial r} + \frac{V_\theta}{r} \frac{\partial(rV_\theta)}{\partial r} + V_z \frac{\partial V_z}{\partial r} - V_z \frac{\partial V_r}{\partial z} \qquad (4)$$

If the inner and outer walls behind the rotor are assumed to be parallel to the axis, so that the radial velocity components may be assumed to be essentially zero, equation (4), when applied outside the rotor where the force term $\mathscr{F}_r = 0$, may be written

$$\frac{\partial V_z}{\partial r} = \left[\frac{\partial H}{\partial r} - \frac{t\partial S}{\partial r} - \frac{V_\theta}{r} \frac{\partial(rV_\theta)}{\partial r} \right] \frac{1}{V_z} \qquad (5)$$

The solution of equation (5) may be carried out with a satisfactory degree of accuracy after the desired degree of tip diffusion is fixed. For the current design, a relative blade-exit Mach number at the tip M'_3 of 0.80 was selected. The corresponding inlet relative Mach number M'_2 at the tip is known from the inlet velocity diagrams. The blade relative stagnation conditions may then be found; and, from the assumed blade relative Mach number, rotational speed, and absolute tangential velocity $V_{\theta,3}$ at the second-rotor exit (from work input), the components of relative and absolute velocity may be found. The stream conditions at the tip may then be computed in their entirety.

If a small portion w (20% in this case) of the total weight flow is selected corresponding to the flow through the small annulus bordered by the tip radius and an adjacent radius a small distance inward Δr, the following continuity expression is approximately satisfied:

$$w \approx 2\pi\bar{r}\Delta r\rho V_z \tag{6}$$

If $\bar{r} = (r_n + r_{n+1})/2$ and $\Delta r = r_n - r_{n+1}$, the next radius is closely approximated by equation (6) as follows:

$$r_{n+1} = \sqrt{r_n^2 - \frac{w}{\pi(\rho_3 V_{z,3})_n}} \tag{6a}$$

Once r_{n+1} and the corresponding increment of weight flow are known, $(rV_\theta)_3$ at that point may be found for the previously fixed work input as a function of w, using the following form of the energy equation:

$$(rV_\theta)_4 = \frac{c_p}{\omega}(T_3 - T_2) + (rV_\theta)_{2a} \tag{7}$$

where the subscript 2a refers to conditions at the second-rotor inlet at the corresponding increment of weight flow.

All the quantities on the right side of equation (5) will be known at points n (tip) and n+1, since H and S are given functions of w at blade exit. Thus, the partial derivatives with respect to r can now be approximated as follows. For small Δr,

$$\left.\begin{aligned}
\frac{\partial H}{\partial r} &\approx \frac{\Delta H}{\Delta r} \\[1em]
\frac{\partial S}{\partial r} &\approx \frac{\Delta S}{\Delta r} \\[1em]
\frac{\partial(rV_\theta)}{\partial r} &\approx \frac{\Delta(rV_\theta)}{\Delta r}
\end{aligned}\right\} \tag{8}$$

Then $\frac{\partial V_z}{\partial r} \approx \frac{\Delta V_z}{\Delta r}$ and V_z at n+1 are readily found and the velocity diagram can be completed. (It should be noted here that the entropy and enthalpy referred to in eq. (5) are the total values contributed by both the first and second stages.)

A source of inaccuracy in this procedure arises from use of the tip conditions in computing r at station n+1 (in eq. (6a)) rather than the more appropriate average tip annulus conditions. This inaccuracy may be reduced either by using smaller increments or by using the first value of r_{n+1} as a first approximation and repeating the calculation to get a second value of r and n+1. On occasions a Taylor expansion for the tip incremental weight flow in terms of r has been used to avoid iteration (ref. 4). Whichever procedure is used, it may be continued stepwise along the radius until the percent weight flow w equals the design value w_{tot} and the corresponding rotor hub radius at the exit is determined.

Rotor hub surface. - The rotor hub surface, while not yet entirely fixed, has four conditions specified, namely, the inlet and exit radii and the hub slope ($dr/dz = V_r/V_z$) at each of these positions. The following third-degree polynominal satisfying these conditions was therefore arbitrarily specified to define the hub contour, starting at $z = 0$ in figure 1:

$$r = -13.6083z^3 + 4.7028z^2 + 0.200z + 0.427 \tag{9}$$

Blade camber line. - While there are available procedures less approximate than the present one (e.g., matrix, relaxation, or stream-filament) whereby the hub contour and blade shape of rotors of this type may be computed, the time required and the necessity for several lengthy iterations eliminated these procedures from consideration. The blade design method utilized herein, while requiring some reiteration, was relatively straightforward and could be carried out quickly. The method is basically that of reference 5. The blade mean section (on mean-radius surface of revolution) was designed on the basis of the mean inlet and exit velocity diagrams, the hub-tip average entropy increase, and the work input across the rotor. The blade hub- and tip-section mean camber lines were then specified as second-degree curves that satisfied the inlet and exit blade angles fixed by these velocity diagrams plus zero rates of change of $\varkappa'$ at the exit. (The latter condition was imposed from consideration of unloading characteristics.) For the relatively high solidity used (20 blades), incidence and deviation angles were assumed to be zero. The mean-section distribution of tangential thickness was later applied to the hub and tip meanlines. A layout of the blade mean section, explaining the nomenclature used, is given in figure 3.

The blade physical characteristics to be determined for the mean radius were the blade angle $\varkappa'$ (except at the leading and trailing edge) and the thickness distribution τ or τ_θ. These characteristics are then to be adjusted to satisfy continuity through control of the passage area and density (density is a function of enthalpy rise and the turning angle). A linear variation in entropy from the inlet to the exit value was assumed in computing ρ. Because knowledge of the pressure- and suction-surface pressures (or velocities) allows the best estimation of loss characteristics, the blade computations were initiated by specification of the blade mean-section loading (pressure- and suction-surface static pressures). The static-pressure difference Δp_θ across the passage was then fixed, which determined also the mean static pressure for the assumption of a linear pressure variation from suction to pressure surface. The initial assumed loading is given by the solid line in figure 4.

On the basis of the assumed loading, a solidity term σ_z (defined as the ratio of axial depth of the blade to blade spacing) required to

give the fixed total work input may be found from a stepwise solution to the following equation derived in reference 6:

$$\sigma_z = -\frac{\gamma \dfrac{\rho_2}{\rho_{a,2}} \dfrac{V_2'}{a_{a,2}} \cos \varkappa_2' \left(\dfrac{r_3}{r_t} \dfrac{V_{\theta,3}}{a_{a,2}} - \dfrac{r_2}{r_t} \dfrac{V_{\theta,2}}{a_{a,2}} \right)}{\displaystyle\int_{\frac{z}{z_{tot}} = 0}^{\frac{z}{z_{tot}} = 1.0} \dfrac{\Delta p_\theta}{p_3} \dfrac{b}{b_2} \dfrac{\bar{r}}{r_t} \, d\!\left(\dfrac{z}{z_{tot}} \right)} \tag{10}$$

Now from definition, $\sigma_z = z_{tot}/(2\pi\bar{r}/n)$ and the number of blades n may be immediately determined. If n is unreasonably large or small or does not approximate an integer, the loading diagrams may be altered systematically and quickly until the desired number of blades n results. The equation for σ_z may now be applied stepwise between the inlet and the successive station along z with the subscript x replacing 3 and (z/z_x) replacing $z/z_{tot} = 1.0$ on the integral. In this manner V_θ is found corresponding to the final loading. The computations may now proceed directly to completion through the use of the following thermodynamic relations for perfect gases and the trigonometric relations between the velocity components:

$$\bar{t} = \bar{t}_2 \left(\frac{\bar{p}}{p_2} \right)^{\frac{\gamma-1}{\gamma}} \left(e^{\Delta S/R} \right)^{\frac{\gamma-1}{\gamma}} \tag{11}$$

$$\bar{T} = \bar{T}_2 + \frac{\omega}{c_p} \left[\overline{(rV_\theta)} - (\overline{rV_\theta})_2 \right] \tag{12}$$

The blade meanline orientation in cylindrical coordinates may now be computed from the variation in $\varkappa'$ with the following relations:

$$\Delta \Theta \bigg]_{x-1}^{x} \approx \frac{\tan \varkappa_x' \, 2\Delta z}{r_x + r_{x-1}} \tag{13}$$

$$\Theta_x = \sum_{z=0}^{z=x} \Delta \Theta \tag{14}$$

The blade mean camber line is thus defined by the three coordinates z, r, and Θ.

Correction of velocities near sonic. - The tentative blade thickness τ was obtained from the following form of the continuity equation:

$$\frac{g\overline{\rho V_z}}{R\overline{t}} \left[\pi(r_t^2 - r_h^2) - \frac{n\tau}{\cos \varkappa'} (r_t - r_h) \right] = w_{tot} \tag{15}$$

There is still, however, a source of error of indeterminate significance involved in the use of the mean axial velocity $\overline{V_z}$ in the equation. The actual weight-flow capacity of a blade passage of given small span is given by the integrated value of ρV_z across the passage. The Mach number range between the suction and pressure force is often of a level wherein $M_s > 1.0$ and $M_p < 1.0$. Under these conditions the mean Mach number may approach 1.0, leading to significant overestimation of the passage flow capacity. The following procedure, which for simplicity assumed a linear variation of relative Mach number (instead of pressure) across the passage, is used in correcting the blade thickness for errors in flow capacity. The ratio of the actual weight flow to the maximum possible is obtained by integrating $\rho V/\rho_a a_a$ across the passage. The resulting expression is

$$\left(\frac{\rho V}{\rho_a a_a}\right)_{int} = \frac{-2.16}{\Delta M}\left[\frac{1.0}{(1.0 + 0.20\ M_p^2 + 0.40\ M_p\Delta M + 0.20\ \Delta M^2)^2} - \frac{1.0}{(1.0 + 0.20\ M_p^2)^2}\right] \tag{16}$$

where $\Delta M = M_s - M_p$.

The ratio $\rho V/\rho_a a_a$ is also obtained for the mean passage Mach numbers $(M_p + M_s)/2$. The ratio of the weight flow actually passed to that computed from the mean Mach number is then given by the expression

$$\frac{\left(\frac{\rho V}{\rho_a a_a}\right)_{int}}{\left(\frac{\rho V}{\rho_a a_a}\right)_{\overline{M}}} = \zeta \tag{17}$$

The blade thickness τ_θ in the tangential direction is now corrected as follows:

$$\tau_{\theta,corr} = \tau_{\theta,o} - \left[(1.0 - \zeta)\left(\frac{2\pi r}{n} - \tau_{\theta,o}\right)\right] \tag{18}$$

To be consistent with previous assumptions, a linear cross-passage variation of static pressure rather than Mach number should be used in computing ζ. However, a lengthy series expansion is required in order to

integrate the resulting expression, leading to values hardly more accurate than the linear Mach number assumption. A final loading for the modified-thickness blades is given by the dashed line of figure 4.

APPARATUS

The test rig used in the performance evaluation was constructed especially for this series of tests and is described fully in reference 1. The setup is shown schematically in figure 5. Instrumentation stations shown in figure 5 are basically the same as for the single-stage tests, with the addition of a survey station 1 inch behind the second rotor (station 3). It was impossible to mount static taps on the inner wall at station 2 between rotors for these tests without resorting to rotating pressure seals or some similar device. Also, there was insufficient room between rotors for a conventional static-pressure probe. Static pressures at station 2 were faired in from the outer-wall readings similarly to the method used to determine the profiles in single-stage tests.

A photograph of the instruments used for these tests is given in figure 6. The combination probes were different from those used in the single-stage tests, having the iron-constantan thermocouple and total-pressure probe enclosed with a central shield. This thermocouple was less sensitive to radial-flow components than the bare-wire type used previously.

The second-stage rotor, which had 20 blades, is shown in the photograph of figure 7.

OPERATING PROCEDURE

For all speed combinations, the speed of the rotor was based on the inlet temperature at station 0. All speeds are presented in percentage of the design equivalent rotational speed $N/\sqrt{\theta}$, which was 18,050 rpm for each rotor. Speed changes were made with the outlet throttles fully open to the laboratory exhaust system.

After test points were obtained at the open-throttle position, the butterfly valves at the collector outlets were closed gradually until shock waves formed in the diverging annulus behind the second rotor. Slight additional throttling forced the shock up onto the straight annulus and into the rotor at low speeds. At high speeds it was not possible to stabilize the shock in the rotor.

In these tests a refinement of operating technique was used with good results. When axial Mach numbers are close to sonic, the immersion of survey probes often affects the location of the normal-shock wave by

changing the flow area. For these tests all instruments were duplicated and operated in pairs, with one survey starting at the inner wall and working outward and the other starting at the outer wall and moving inward. In this way, the total frontal area of the instruments was kept constant at all times.

RESULTS AND DISCUSSION

Over-All Performance

The characteristic map of the over-all performance of the two counterrotating rotors at the same speed is given in figure 8. The peak design-speed pressure ratio was 4.3, obtained at a specific equivalent weight flow of 27.2. From this map it is apparent that the operating range at each tip speed is very limited. At the lower speeds some range of weight flow exists, and it is possible to apply back pressure to the second rotor by throttling outlet flow without forcing the operation into surge. At high speed, back pressure may be applied up to the point where a shock is stabilized in the annulus at the rear of the rotor; but, when an attempt is made to force the shock inside, the unit is thrown into surge. As a result of this behavior, the over-all performance has the characteristic that weight flow is virtually unique with speed, and a single rotor operating point is found.

When the speed ratio between spools is varied, the characteristic maps shown in figure 9 result. When these maps are superimposed on figure 8, the curves overlap as shown in figure 9(f). Thus, it is possible to reach the same pressure ratio and weight flow by a variety of combinations of rotor speed. At high speed, however, it is not possible to reach a different weight flow at a given pressure ratio by changing speeds.

The over-all adiabatic efficiency corresponding to the characteristic maps just discussed is given in figure 10. The best adiabatic efficiency obtained was 0.75. When both rotors are at equal speeds, the efficiency is fairly low but quite uniform with speed. For the unequal combinations of speed, again the curves coincide with the equal-spool speeds over most of the weight-flow and speed range.

Matching of Rotors

The operation of the first-stage rotor when the second rotor is installed is shown in figure 11. The solid lines of this figure present the standard characteristic map of the first stage as determined in the tests of reference 1, the heavier line representing the stall-limit line as determined in these tests. At equal rotor speeds of the two-stage configuration the maximum flow (dash-dot line and solid symbols) is in

the previously determined stall region of the first-stage rotor at most speeds. Under these conditions, however, the stall instrumentation did not exhibit a periodic stall; instead, a random fluctuation of similar magnitude was found behind the second rotor.

Because each rotor was driven by its own motor and gearbox, it was possible to obtain a wide variety of speed combinations. There was no point in operating the first rotor at speeds higher than the second, because this forced the first rotor farther into the stall region, as shown by the point in figure 11 for 80-percent first-rotor speed and 70-percent second-rotor speed. When the first-stage speed was held constant and the second-stage speed was increased, the inlet equivalent weight flow increased, moving the first-stage operation out of stall. By increasing the second-stage speed to 100 percent with the first stage at 50 percent, and then accelerating the first stage to 100 percent, it was possible to circumvent the stall region entirely. There was no apparent difference in performance at design speed due to the method of approaching the operating point.

Another fact brought out by figure 11 is the mismatching of weight-flow capacity between rotors at design speed. The low maximum weight-flow capacity of the second rotor at design speed forces the first rotor to operate at the surge point, where efficiency is less than optimum. At lower speeds the operating points are even farther from the peak-efficiency point. The weight flow of 27.2 pounds per second per square foot frontal area, obtained with both rotors at design speed, is considerably below the value of 29.2 pounds where peak efficiency of the first stage occurred. A shift of the design-speed match point to 29.2 pounds per second per square foot would probably allow operation out of the stall region at all speeds, although first-stage efficiency would be low.

Static-Pressure Profiles on Outer Casing

First rotor at 50-percent design speed. - In figure 12(a) the ratio of static pressure at the outer casing to the total pressure at station 0 is plotted as a function of axial distance. The locations of the leading edges and trailing edges of both rotors, as well as the instrument stations, are identified on the figure. Static-pressure profiles are presented for open-throttle or choke points where the speed of the first rotor is held constant and the speed of the second rotor is varied. The equivalent weight flow at the entrance to both rotors is given in the figure key.

As might be expected, the static-pressure profile over the first rotor shows only the change associated with varying the weight flow over

a fairly wide range. With the first rotor at 50-percent speed, the static-pressure rise is rather small but does show the type of operation characteristic of throttled flow shown in reference 1. Between the rotors, the static pressure is relatively uniform, the slight decrease resulting from the small convergence of area.

At the second rotor, the static pressure increases sharply, indicating the presence of a shock configuration at the channel entrance. This shock is skewed with respect to the axis of rotation; otherwise, the pressure would be more abrupt. As the second-rotor tip speed is increased, the inlet relative Mach number is increased and the static pressure rises accordingly. At the open-throttle position the relative flow accelerates in the rear of the rotor, causing the drop in static pressure shown. The second rotor was followed by a 4-inch-long straight annulus. As shown in the key, the equivalent weight flow into the second rotor increases with second-rotor speed, indicating that the flow limitation is in the relative rather than in the absolute flow. Further, the fact that the flow can expand supersonically in the rear of the rotor indicates that the area limitation occurs upstream of this point.

Both rotors at design speed. - The same type of static-pressure profile is given in figure 12(b) for operation of both rotors at design speed. At open throttle, sharp pressure rises typical of an external shock configuration may be seen near the leading edge over both rotors. In the second rotor the nonuniform flow accelerates in the rear of the rotor and continues to expand in the tip region behind the rotor until the instrument station is reached. At this point the presence of the instruments probably precipitates a shock.

With the straight annulus, back pressure could be applied to move the shock forward from measuring station 3 for a short time period. This operating point was very unsteady and resulted in surge as soon as the survey instruments were moved. In an effort to stabilize the flow in the vicinity of the measuring station, the inner fairing behind the second rotor was tapered $1\frac{1}{2}^{O}$. Under these conditions it was possible to stabilize a shock just at the rotor outlet, and flow was much more stable at the measuring station. However, it was still impossible to force the shock into the rear of the rotor without throwing the operation into surge. The static-pressure profile obtained with the $1\frac{1}{2}^{O}$ taper on the inner wall and with the downstream shock stabilized at the rotor exit is given by the solid points. Operation of the two rotors was virtually unaffected by the change, and no improvement in over-all performance was noted. Static pressure at measuring station 3, however, was much higher than for the original configuration.

Variation of Flow Area in Second Rotor

A plot of flow area against axial distance for the second rotor is given in figure 13. The original computed flow area is given by the dashed line. Unfortunately, in translating the aerodynamic design into hardware, a small error in the hub profile was made that resulted in the actual area shown by the solid line. All these areas are based on the mean-line blade angle x and thus are not really precise. The trends, however, should be accurate.

A comparison of the profiles of figure 12(a) with the flow areas in figure 13 shows fair agreement between the point where the expansion of flow begins and the increased area available near the rotor exit. Even if the flow area had been made according to the original aerodynamic design, it is doubtful that the design weight flow would have been passed, because the losses in the first rotor were greater than design. No additional blockage allowance was made for the small losses between rotors. In addition, the design of the second rotor was optimistic in allowing for a linear increase in entropy from rotor inlet to exit, when actual losses were concentrated at the inlet because of shock waves.

Radial Variation of Performance Parameters at Rotor Outlet

In figure 14 the radial variations of over-all pressure ratio, adiabatic efficiency, and energy addition are given for two test points at design speed. In addition, the design values are given by the dashed lines. The pressure ratio decreases rapidly from hub to tip and is considerably below design at all radii. At least part of the discrepancy at the tip is due to the poor performance of the first stage along this element, as discussed in reference 1. The same observations hold true for the adiabatic efficiency, which decreases rapidly toward the tip.

It is evident that over-all values of energy addition equal to or greater than design were attained except at the hub. Therefore, the discrepancy in pressure ratio near the tip is purely a result of excessive losses, as reflected by the decreased efficiency. Although the over-all energy addition approximates design near the tip, the influence of the reacceleration in the rear of the second stage is not shown by the over-all energy addition. Actually, as pointed out in reference 1, the energy addition near the tip for the first rotor was considerably above design. Consequently, the second-stage energy addition may be below design, with the result that the over-all condition approximates design.

SUMMARY OF RESULTS

As a result of preliminary tests of a two-stage counterrotating compressor, the following results may be stated:

1. At design speed for both rotors, an over-all total-pressure ratio of 4.3 was obtained at a specific weight flow of 27.2 pounds per second per square foot of frontal area with an adiabatic efficiency of 0.75.

2. Excessive losses in the first rotor and an improper flow-area distribution in the second rotor combined to cause choking in the second rotor at weight flows considerably below design and below the optimum operation of the first stage.

3. Although mismatching of weight-flow capacity between rotors caused the first rotor to operate in the stalled region over most of its range of speeds, no evidence of periodic rotating stall was found at the second-rotor outlet.

4. It was possible to operate the second rotor over a complete range of higher speeds with the first rotor at a fixed speed. Although it was also possible to operate with the first rotor at speeds higher than the second rotor, such operation forced the first rotor farther into the stalled region.

5. At high speeds, it was impossible to stabilize a second shock within the rotor, resulting in operation at a single value of equivalent weight flow at a given speed combination.

6. No significant effects of the second-rotor shock configuration on the first-rotor performance were observed.

7. Additional second-stage area should have been provided by use of a blockage correction in the interrotor annulus.

Lewis Flight Propulsion Laboratory
    National Advisory Committee for Aeronautics
        Cleveland, Ohio, August 1, 1956

REFERENCES

1. Wilcox, Ward W., and Wright, Linwood C.: Investigation of Two-Stage Counterrotating Compressor. I - Design and Over-All Performance of Transonic First Compressor Stage. NACA RM E56C15, 1956.

2. Wilcox, Ward W.: An Analysis of the Potentialities of a Two-Stage Counterrotating Supersonic Compressor. NACA RM E52E01, 1952.

3. Wu, Chung-Hua, and Wolfenstein, Lincoln: Application of Radial-Equilibrium Condition to Axial-Flow Compressor and Turbine Design. NACA Rep. 955, 1950. (Supersedes NACA TN 1795.)

4. Tysl, Edward R., Klapproth, John F., and Hartmann, Melvin J.: Investigation of a Supersonic-Compressor Rotor with Turning to Axial Direction. I - Rotor Design and Performance. NACA RM E53F23, 1953.

5. Stanitz, John D.: Approximate Design Method for High-Solidity Blade Elements in Compressors and Turbines. NACA TN 2408, 1951.

6. Klapproth, John F.: General Considerations of Mach Number Effects on Compressor-Blade Design. NACA RM E53L23a, 1954.

TABLE I. - DESIGN VECTOR DIAGRAMS FOR COUNTERROTATING COMPRESSOR

First stage

Second stage
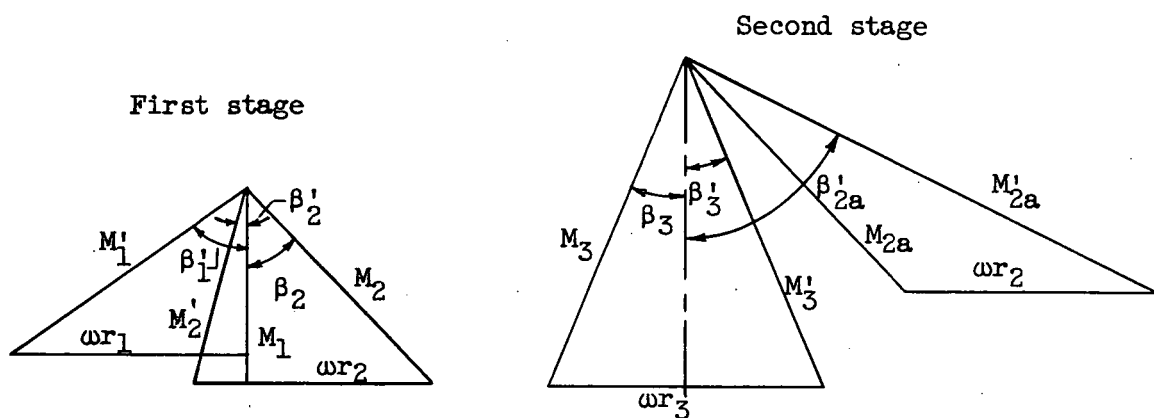
% Flow	100	50	0
M_1	0.572	0.636	0.567
M_1'	.801	1.12	1.29
M_2'	.678	.727	.686
M_2	1.045	.955	.734
β_1'	$45.5°$	$55.4°$	$63.94°$
β_2'	$-16.65°$	$17.76°$	$44.2°$
β_2	$53.58°$	$43.8°$	$47.15°$
r_1/r_t	.500	.786	.996
r_2/r_t	.611	.807	.953
T_2/T_1	1.243	1.243	1.243
P_2/P_1	1.92	2.10	1.72

% Flow	100	50	0
M_{2a}	1.24	1.04	0.777
M_{2a}'	1.83	1.76	1.66
M_3'	.983	1.14	.80
M_3	1.13	1.13	1.15
β_{2a}'	$61.91°$	$63.15°$	$70.36°$
β_3'	$11.96°$	$23.01°$	$24.84°$
β_3	$31.75°$	$22.2°$	$37.6°$
r_2/r_t	.64	.81	.95
r_3/r_t	.84	.89	.95
T_3/T_2	1.412	1.358	1.428
P_3/P_2	2.71	2.65	2.5
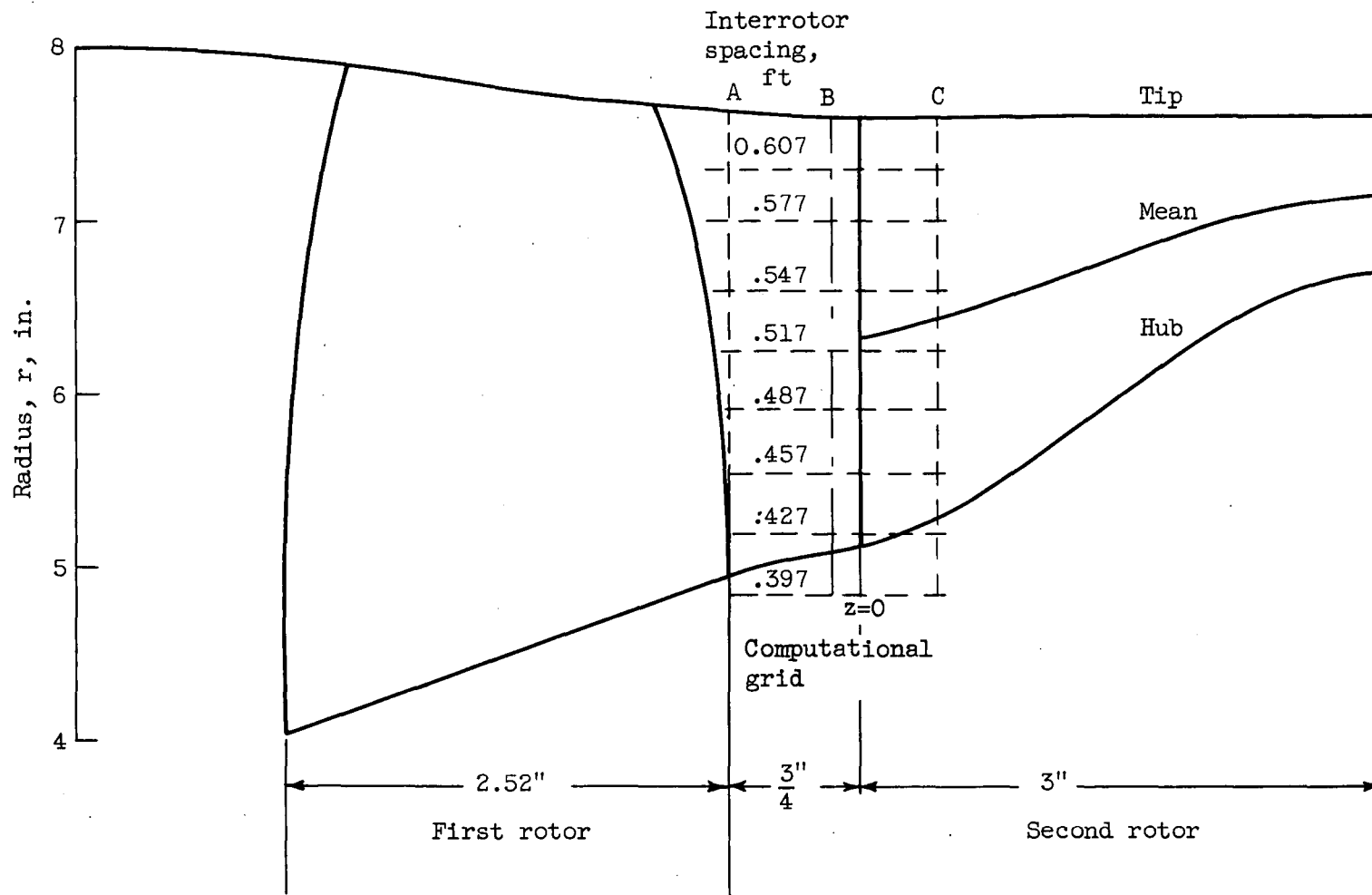
Figure 1. - Schematic sketch of counterrotating compressor in radial-axial plane.
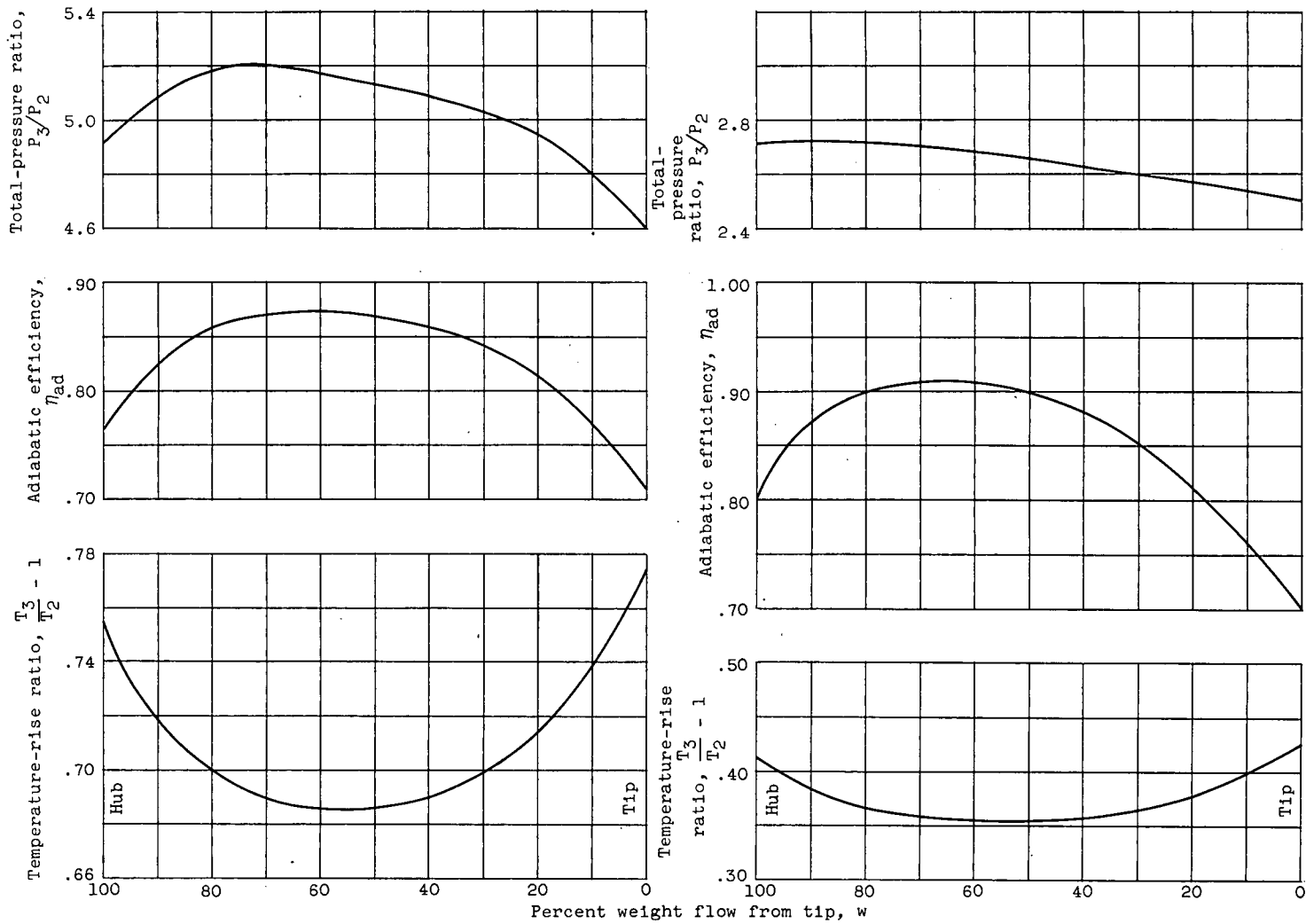
(a) Over-all performance.

(b) Second-rotor performance.

Figure 2. - Performance assumed for counterrotating compressor.
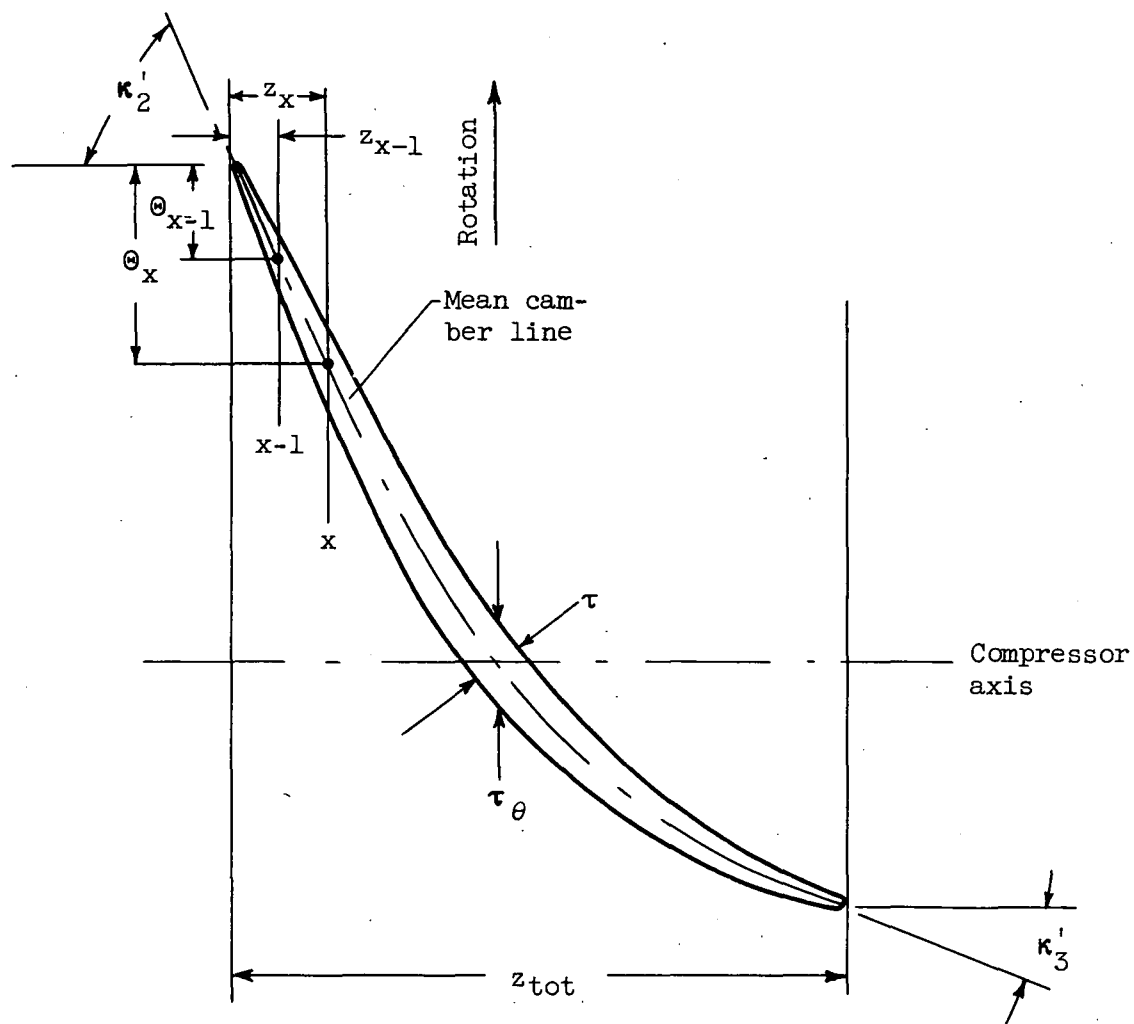
Figure 3. - Second-rotor blade mean section and nomenclature.
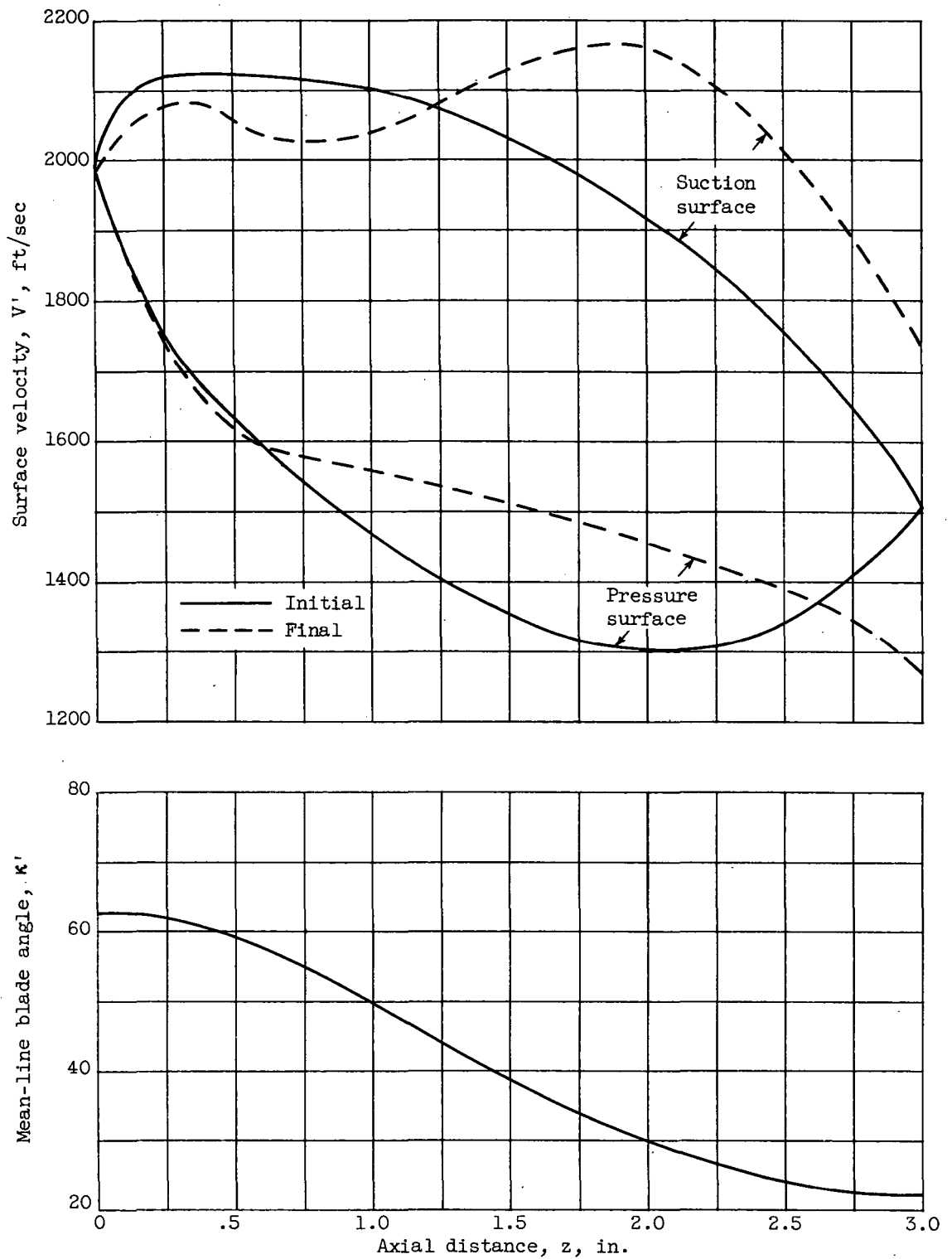
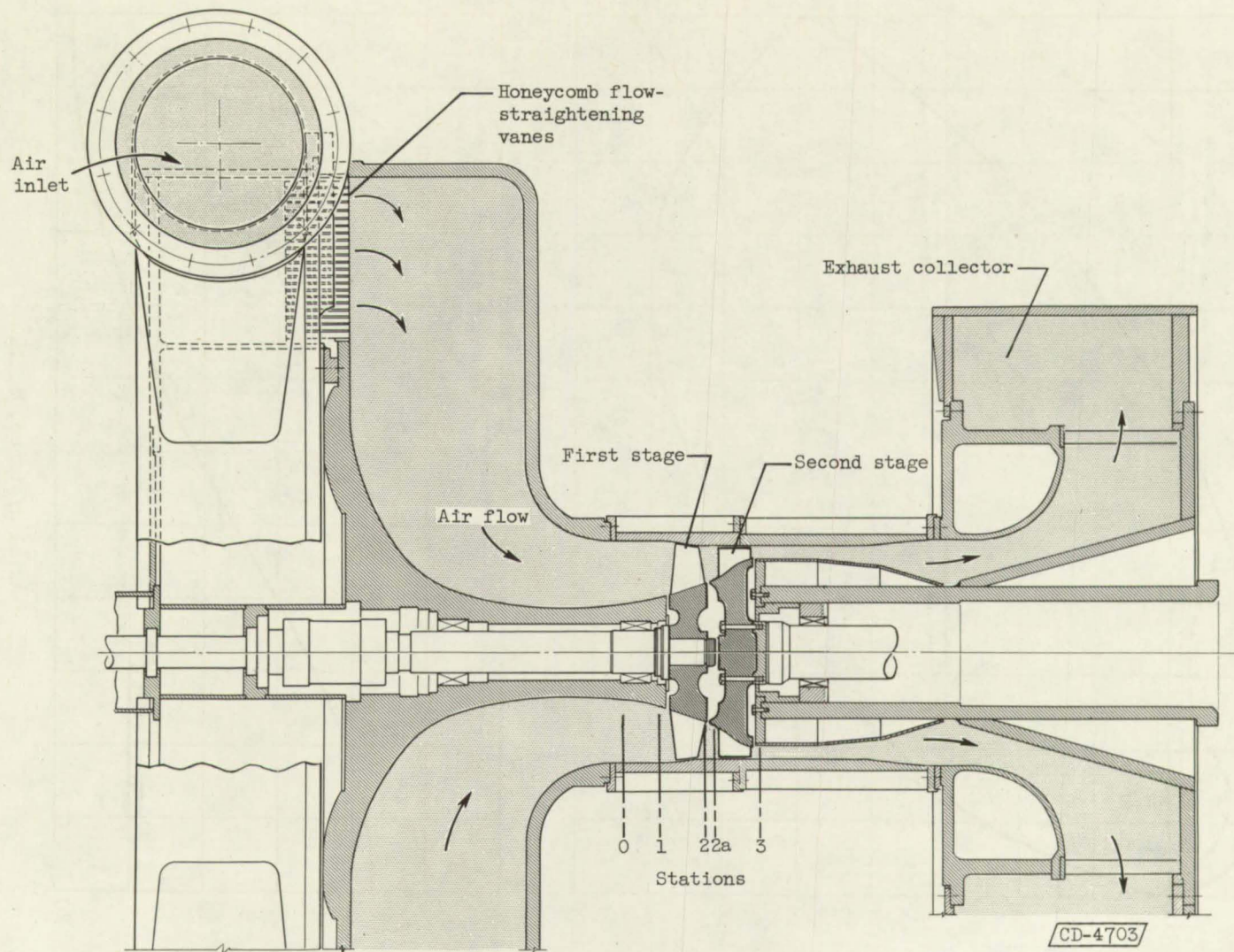Figure 4. - Axial variation of blade surface velocities and blade angles.

Figure 5. - Test rig for counterrotating compressor.
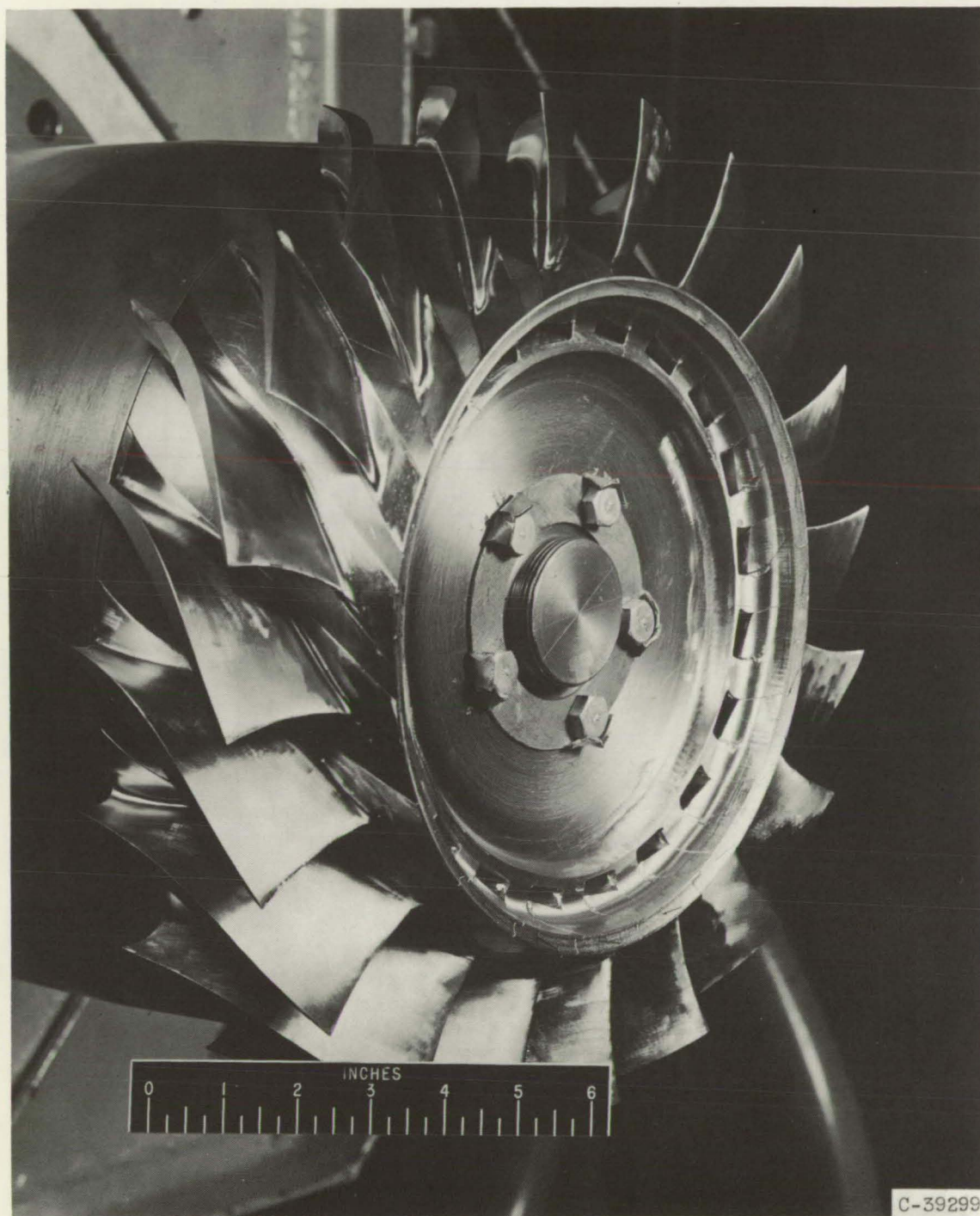
Figure 6. - Combination and L-static probes.

Figure 7. - Second-stage rotor of counterrotating compressor.
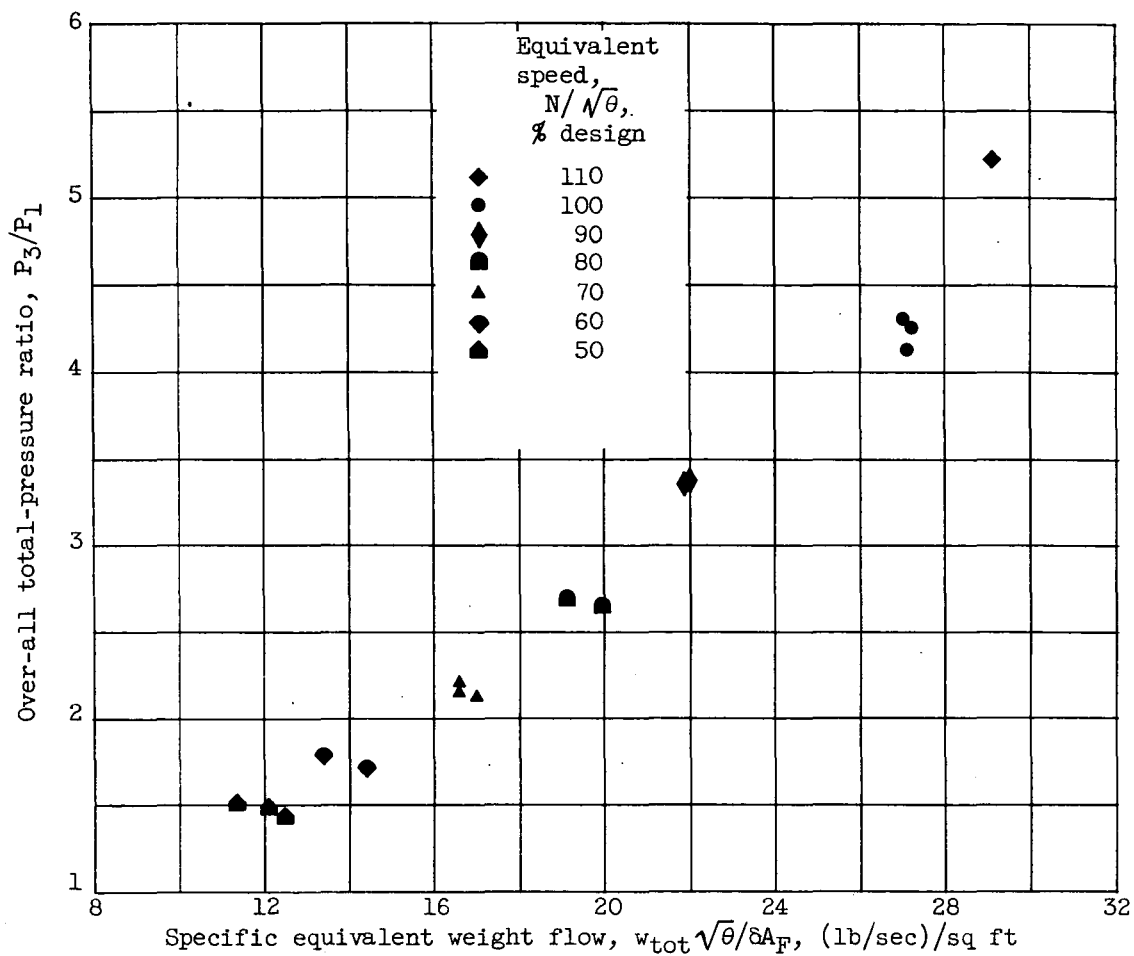
Figure 8. - Over-all performance of counterrotating compressor with both rotors at same speed.

(a) First-stage speed, 50-percent design.

(b) First-stage speed, 70-percent design.

(c) First-stage speed, 80-percent design.

(d) First-stage speed, 90-percent design.

(e) First-stage speed, design.

(f) First and second stages at various speeds.
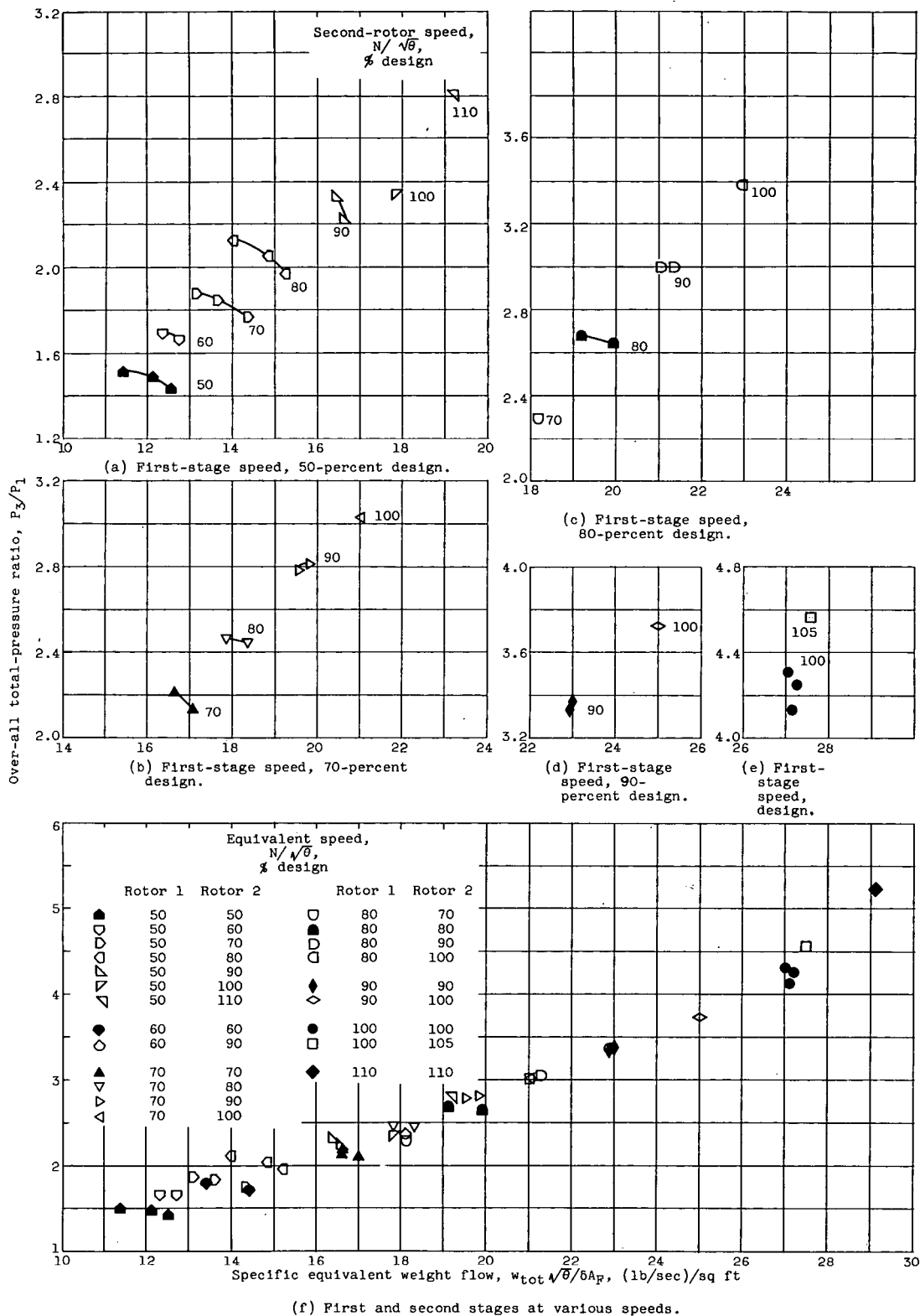
Figure 9. - Performance maps of counterrotating compressor with various combinations of inner- and outer-spool speeds.
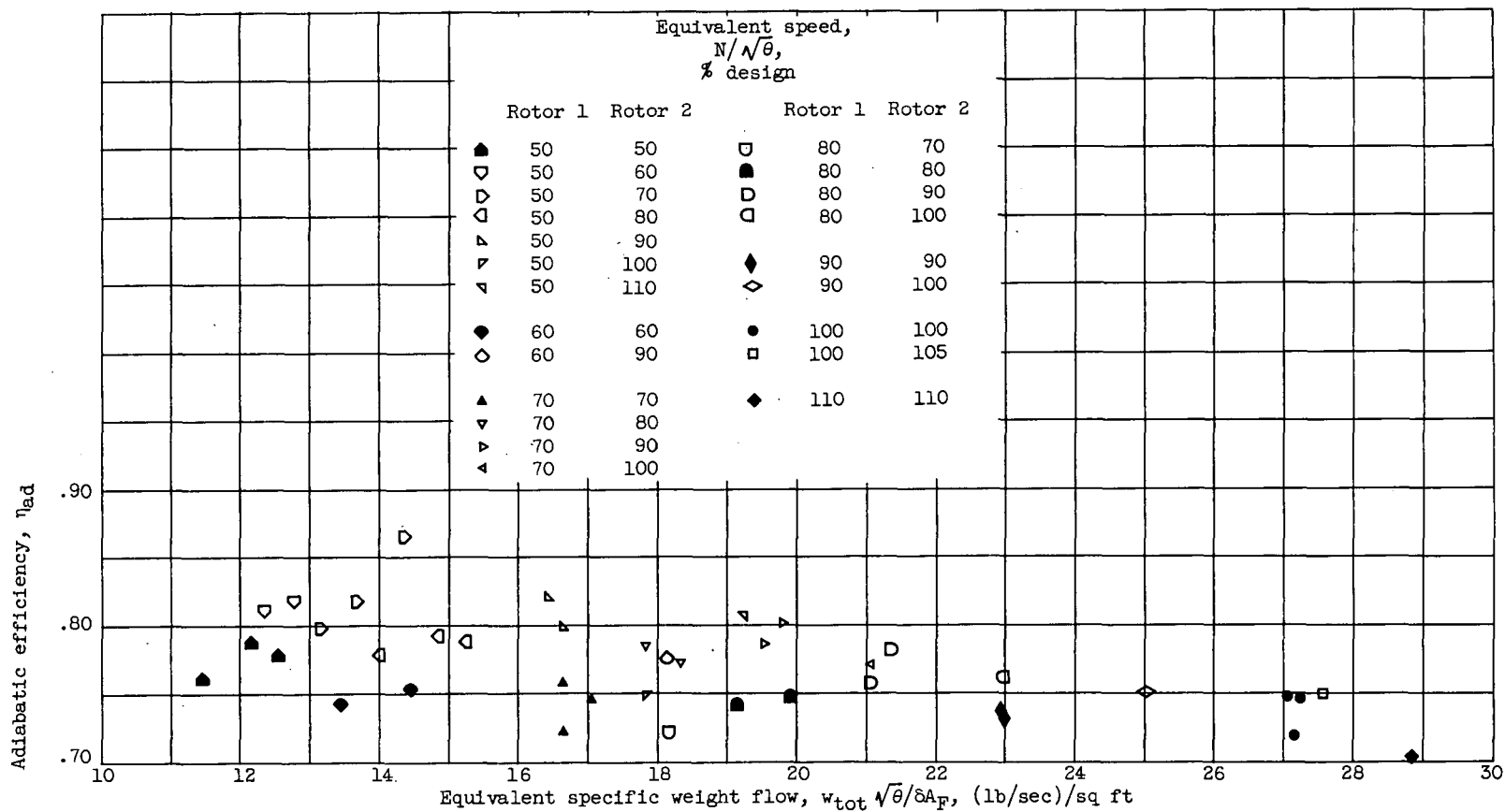
Figure 10. - Over-all adiabatic efficiency for all speed combinations.
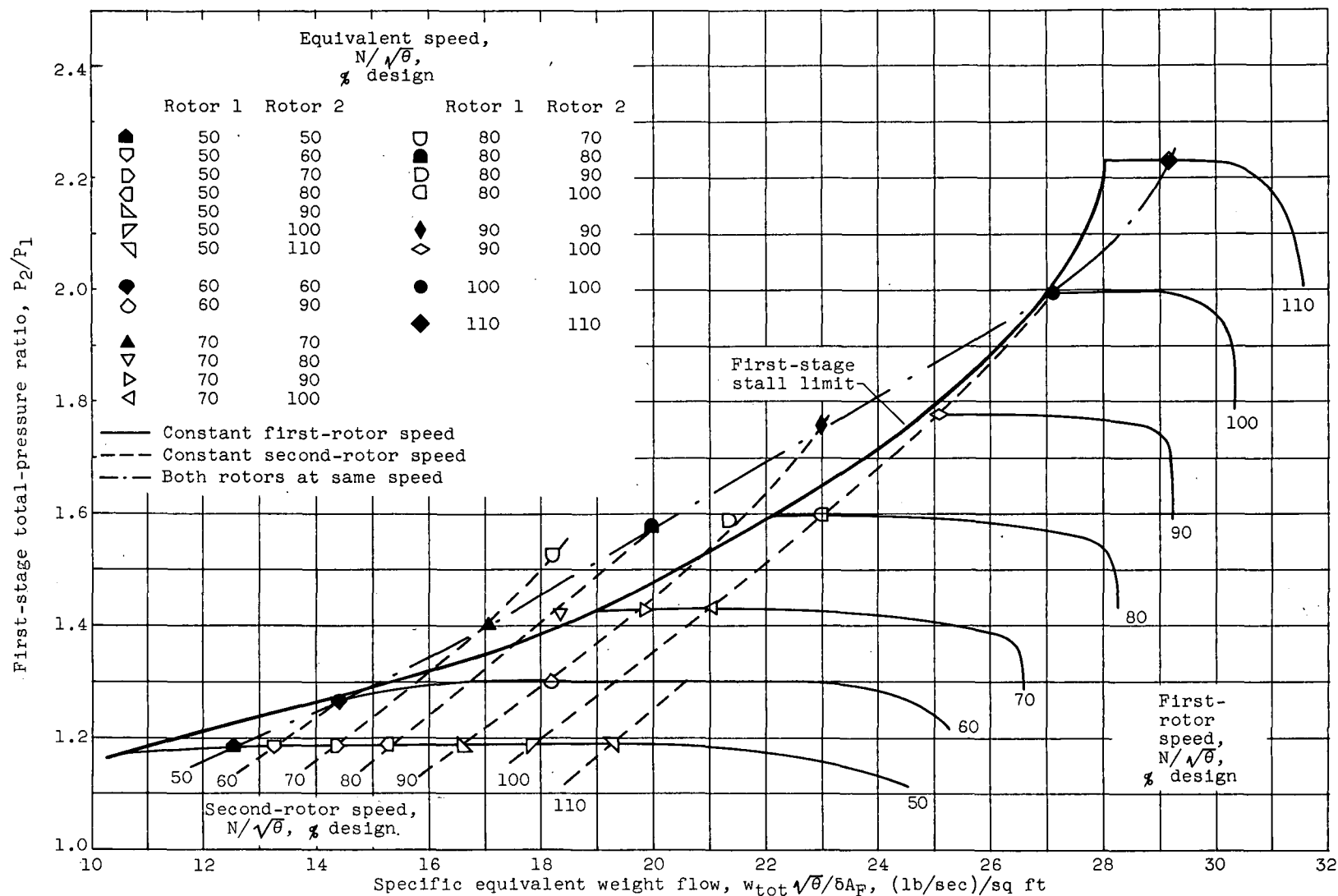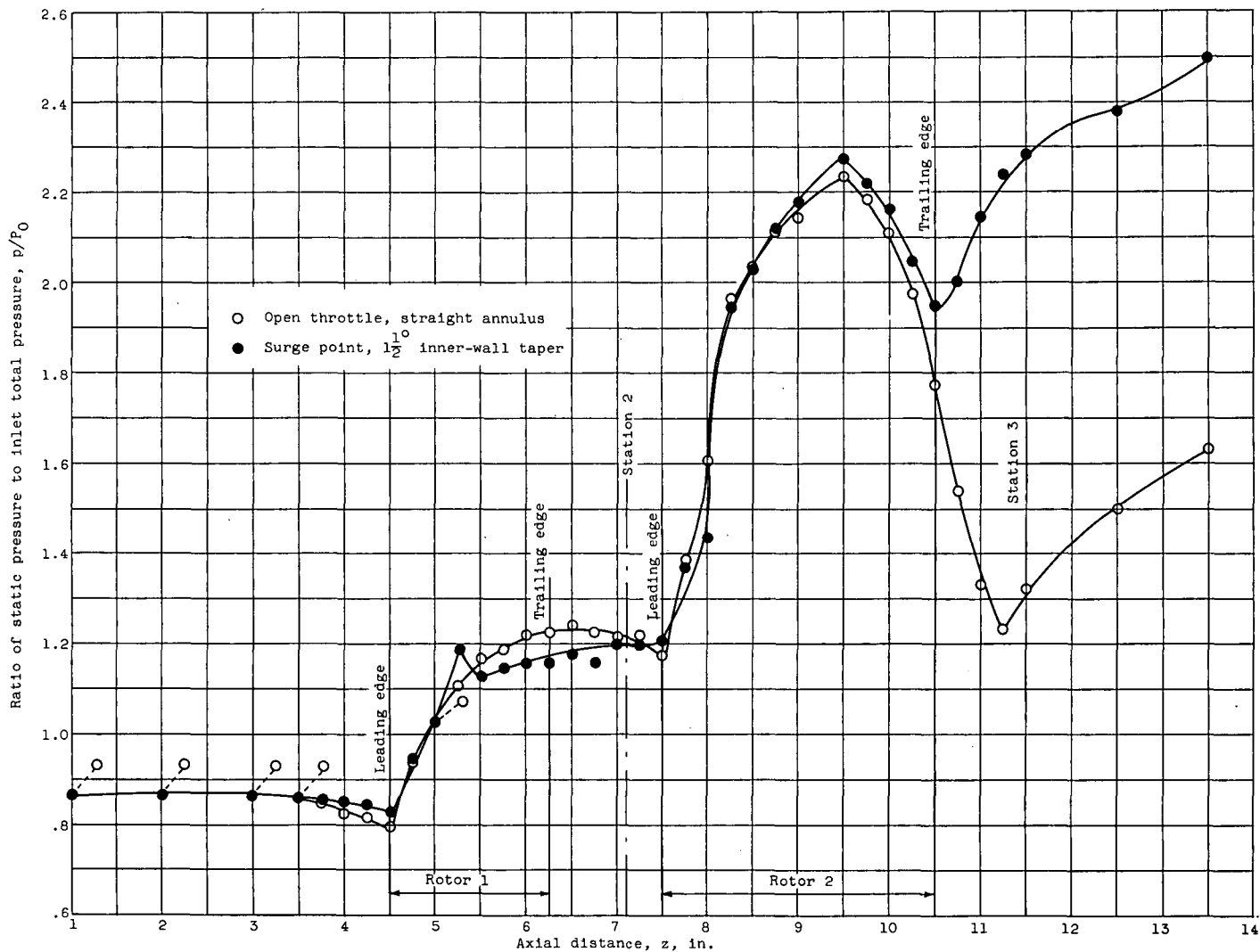
Figure 11. - Performance map of first-stage rotor showing operation imposed by choking in second-stage rotor.
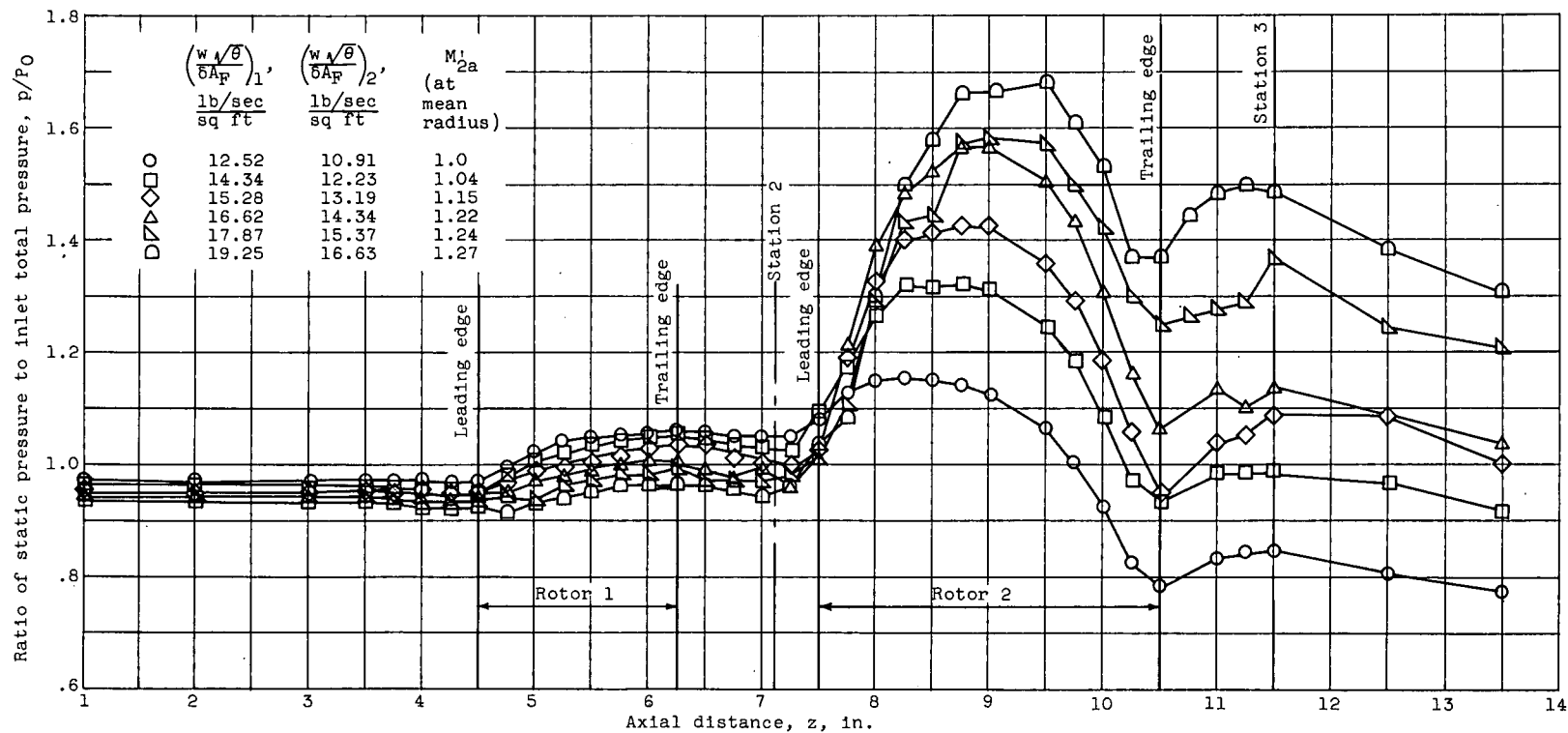
(a) First rotor at 50-percent design speed; second-rotor speed varied (open-throttle points).

Figure 12. - Static-pressure profiles on outer casing.

(b) Both rotors at design speed.

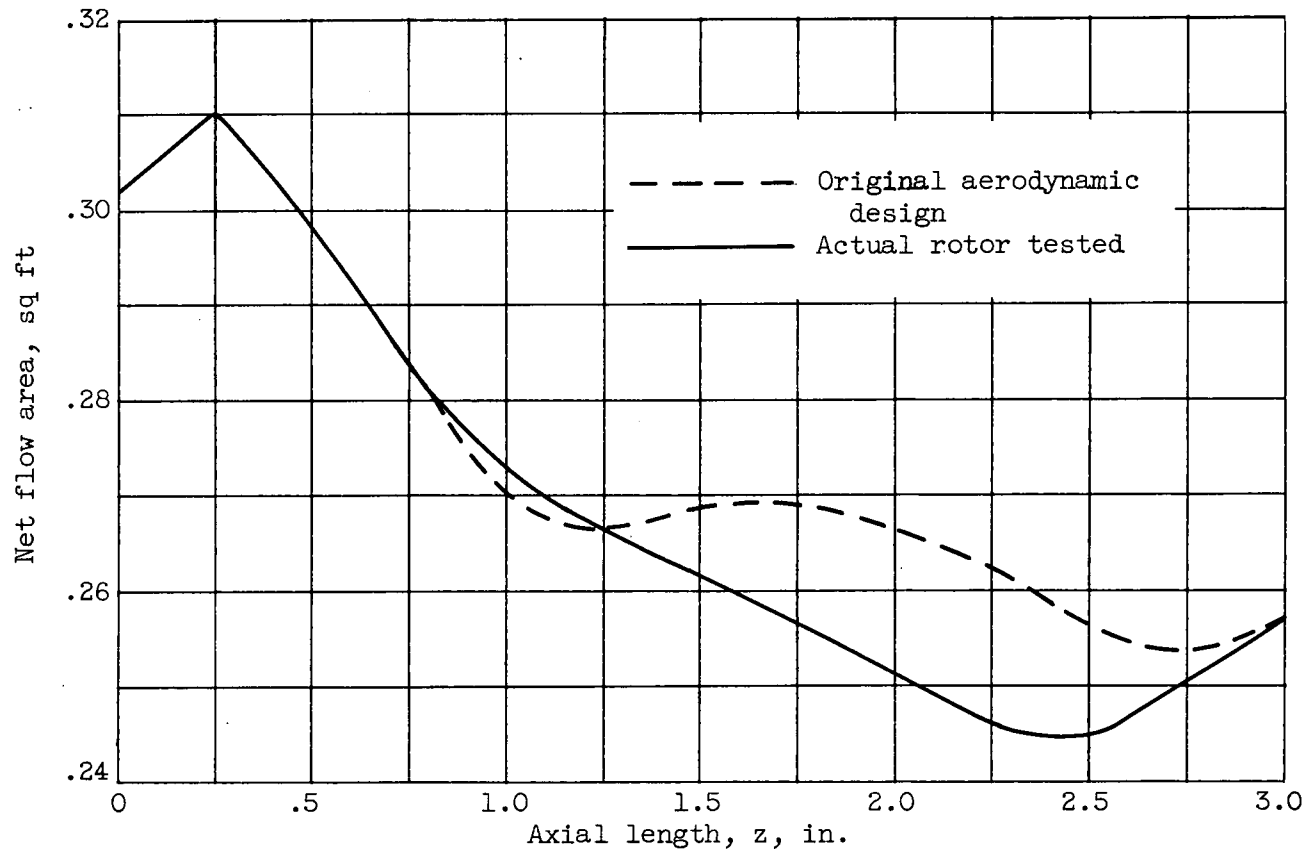Figure 12. - Concluded. Static-pressure profiles on outer casing.

Figure 13. - Axial distribution of net flow area in second rotor.
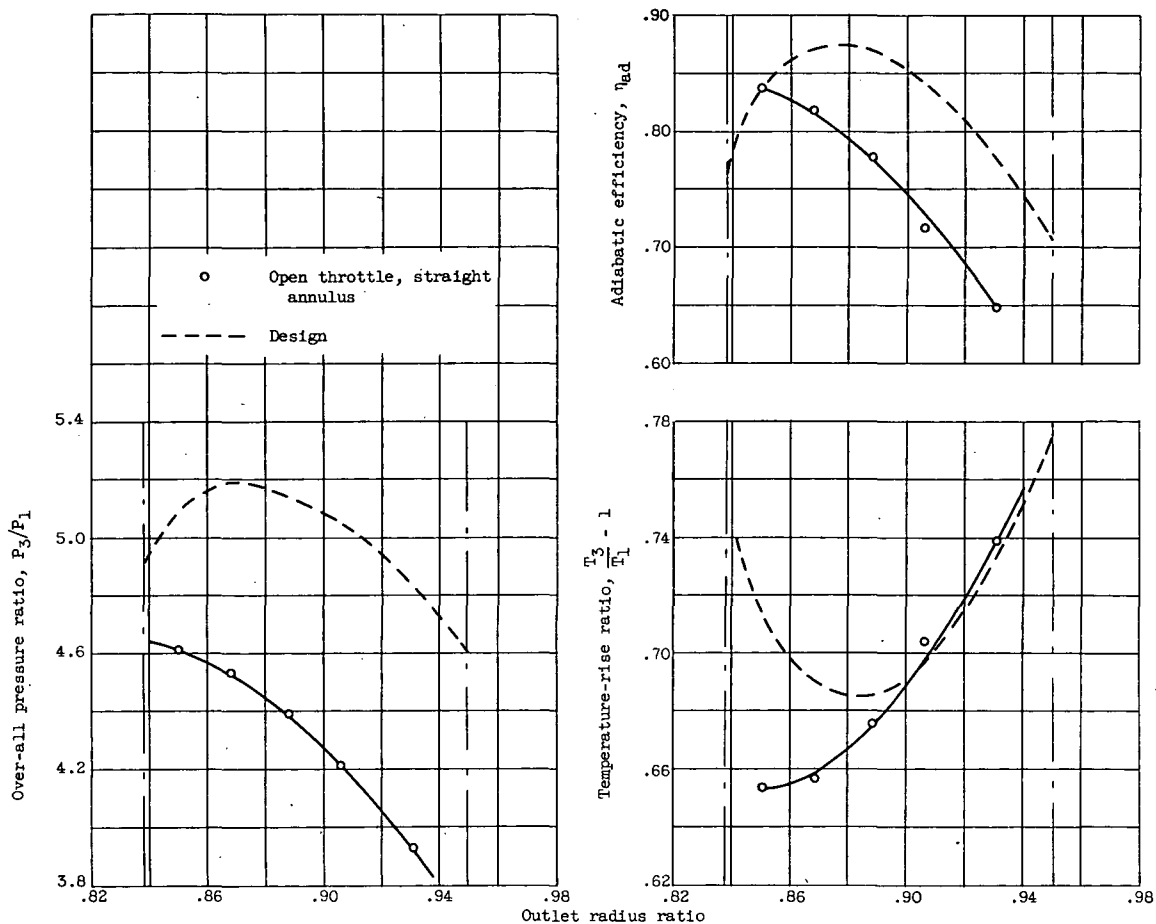
CONFIDENTIAL

Figure 14. - Radial variation of outlet conditions for counterrotating compressor at design speed.

CONFIDENTIAL